Electronic Supplementary Material (ESI) for ChemComm.
This journal is © The Royal Society of Chemistry 2024

Electronic Supplementary Information

Sn-based Film Electrodeposited on Ag Foil for Selective Electrochemical CO_2 Reduction to CO

Zixi Fan,[‡ab] Han Yang,[‡b] Dexin Yang,[*b] Hongping Li,[b] Kongsheng Qi,[b] Zhixin Hua,[b] Xiaoyan Jia,[b] Keke Chen[b] and Buxing Han[*c]

a. Henan Institute of Advanced Technology, Zhengzhou University, Zhengzhou 450003, China

b. Green Catalysis Center, College of Chemistry, Zhengzhou University, Zhengzhou, 450001, China

c. National Laboratory for Molecular Science, Institute of Chemistry, Chinese Academy of Sciences, Beijing, 100190, China

‡ These authors contributed equally.

Corresponding Authors:

E-mail: yangdx@zzu.edu.cn; hanbx@iccas.ac.cn

Experimental Section

Materials

All chemicals and reagents were purchased commercially without further purification. Concentrated sulfuric acid (H_2SO_4) (95%~98%) was purchased from Tianjin Zhiyuan Chemical Reagent Co., Ltd. Acetonitrile (MeCN) was provided by Tianjin Kermel Chemical Reagent Co., Ltd. Ethanol (C_2H_5OH) was obtained from Tianjin Fu Yu Fine Chemical Co., Ltd. Acetone was purchased from Sinopharm Chemical Reagent Co., Ltd. Tin dichloride ($SnCl_2$) was offered by Shanghai Macklin Biochemical Co., Ltd. 1-Butyl-3-methylimidazolium hexafluorophosphate ([Bmim]PF_6) was provided by Lanzhou Institute of Chemical Physics, Chinese Academy of Sciences. Polyethylene oxide-polypropylene oxide-polyethylene oxide (P123) was bought from Beijing InnoChem Science & Technology Co., Ltd. Nafion N-117 proton exchange membrane and Toray carbon paper (TGP-H-60) were purchased from Alfa Aesar (China) Chemical Co., Ltd. Carbon dioxide (CO_2) was provided by Henan Yuanzheng Special Gas Co., Ltd and nitrogen (N_2) was bought from Henan Boyi New Energy Technology Co., Ltd. The purities of CO_2 and N_2 were 99.999%. The isotope-labelled $^{13}CO_2$ (99 at% ^{13}C) was obtained from Sigma-Aldrich Co., Ltd.

The synthesis of Sn/Ag-y electrodes

The Sn/Ag-y electrodes were prepared using a typical electrodeposition method[1, 2] and the detailed preparation is shown as follows. Firstly, Ag foil (1 cm × 1 cm) was used as the conductive substrate and was polished with sandpaper. After polishing, the Ag foil was immersed in 10 mL of H_2SO_4 (0.5 M) aqueous solution for ultrasonic treatment to remove the superficial oxide layer and impurities. After 30 min of ultrasonic treatment, the Ag foil was rinsed with H_2O and ethanol, and then dried in a vacuum drying oven. Secondly, a certain concentration of $SnCl_2$ (10 mM, 15 mM, 20 mM, and 30 mM), 0.5 M of H_2SO_4 aqueous solution (1 mL) and H_2O (30 mL) were in sequence added into a 50 mL beaker with 10 min of ultrasonic treatment to ensure complete dissolution. Then, 0.06 wt.% of P123 was added to the above solution. After 20 min of ultrasonic treatment, the resulting solution was placed in the electrodeposition bath. Thirdly, a three-electrode system with Ag foil as the cathode, Pt mesh as the anode, and Ag/AgCl as the reference electrode was used for the electrodeposition process. The electrodeposition experiments were performed at -0.8 V vs Ag/AgCl for 200 s. Subsequently, the obtained electrodes were rinsed multiple times with ethanol and H_2O, and then immersed in ethanol overnight to remove residual electrodeposition solution and surfactants. Finally, the resulting electrodes were dried in a vacuum drying oven. The above electrodes were named Sn/Ag-y electrodes, where y represented the concentration of Sn^{2+} in the electrodeposition bath.

Characterizations

The morphologies of different Sn/Ag-y electrodes were observed by a Care Zeiss SIGMA 500 SEM and a Tecnai G2 F20 TEM equipped with the energy-dispersive X-ray energy spectroscopy (EDX). The XRD patterns of different Sn/Ag-y electrodes were obtained on an X'Pert PRO X-ray diffractometer with Cu-Kα radiation at a scan speed of 3 °/min to study their crystal structures. The XPS spectra of various Sn/Ag-y electrodes were measured on the Thermo Scientific ESCALab 250Xi with a 200 W monochromatic Al-Kα resource and the base pressure in analysis chamber was approximately 3×10^{-10} mbar.

ECR reactions

All ECR reactions were carried out on Shanghai Chenhua CHI 6081E electrochemical workstation in an H-cell. A three-electrode system comprised a counter-anode (Pt mesh), a working electrode (Sn/Ag-y electrodes or pure Ag foil), and a reference electrode (Ag/Ag^+). The anode and cathode compartments were separated by a proton exchange membrane. The electrolyte in the anode compartment consisted of H_2SO_4 aqueous solution (0.5 M, 30 mL), while the cathode compartment contained a mixed solution of [Bmim]PF_6, H_2O, and MeCN (30 mL). Before starting the electrolysis experiments, a steady flow (20 mL min^{-1}) of CO_2 was bubbled into the above electrolytes, and magnetic stirring was maintained for approximately 30 minutes to ensure the saturation of the solution with CO_2. All CPE experiments in this study were carried out at standard pressure and room temperature.

C_{dl} measurements

The ESCA and C_{dl} values exhibit a positive correlation, according to the Randles-Sevcik formula[3]. In [Bmim]PF_6 (30 wt.%)/H_2O (5 wt.%)/MeCN electrolytes, a series of CV curves were obtained by adjusting the scanning rate in the applied potential range of -1.85 ~ -1.95 V vs. Ag/Ag^+.

EIS measurements

The EIS measurements were performed in [Bmim]PF_6 (30 wt.%)/H_2O (5 wt.%)/MeCN electrolytes. Nyquist plots of Sn/Ag-y electrodes were measured at an open circuit potential with a frequency of 10^{-2} ~ 10^6 Hz.

Product analysis

After CPE experiments, the gaseous and liquid products were collected separately. The gaseous products were analyzed using a GC (Agilent 8860) equipped with TCD and FID detectors. Liquid products dissolved in dimethylsulfoxide-d_6 (DMSO-d_6) were detected by ^1H NMR (Bruker Avance III 600 HD) using phenol as an internal standard[4, 5]. The Faradaic efficiencies of different products were calculated on the basis of above analysis results.

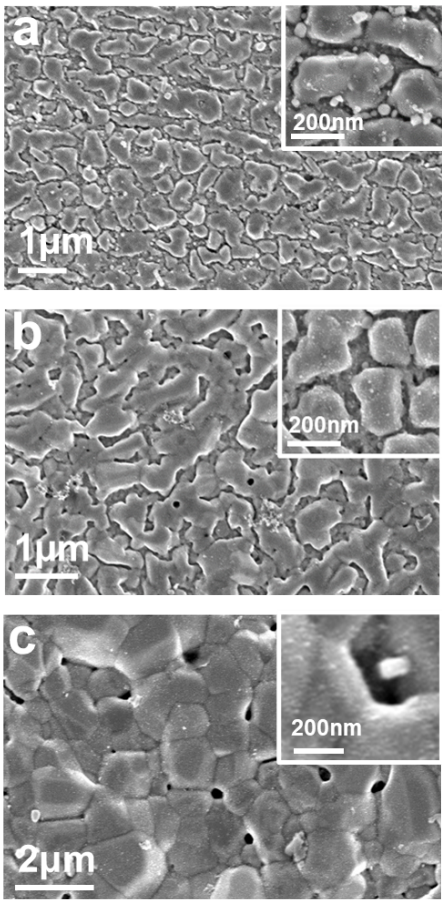

Fig. S1 The SEM images of different Sn/Ag-y electrodes: (a) Sn/Ag-10; (b) Sn/Ag-15; (c) Sn/Ag-30. The insets show higher-magnification images.

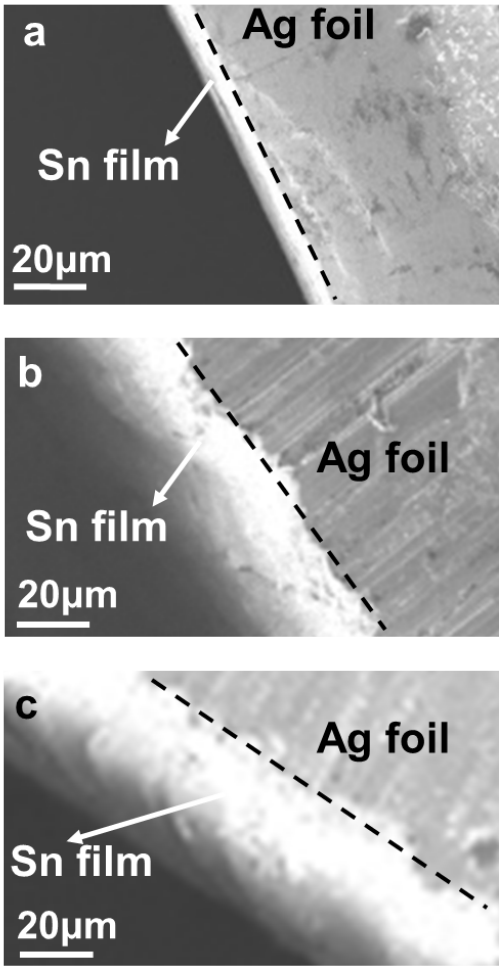

Fig. S2 The cross-sectional SEM images of different Sn/Ag-y electrodes: (a) Sn/Ag-10; (b) Sn/Ag-15; (c) Sn/Ag-30.

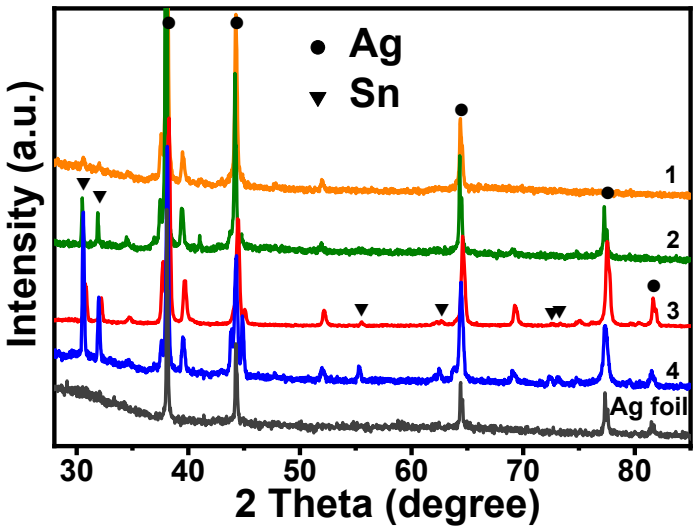

Fig. S3 XRD patterns of different electrodes. The lines of 1, 2, 3, and 4 represent Sn/Ag-10, Sn/Ag-15, Sn/Ag-20 and Sn/Ag-30 electrodes, respectively.

In Fig. S3, the peaks at 37.6°, 39.5°, 51.91°, and 69.0° are attributed to (002), (111), (112), and (113) crystalline planes of the orthorhombic Ag_3Sn (JCPDS No. 04-0800)[6], which may come from the slight interdiffusion of Ag and Sn atoms at the interface[7].

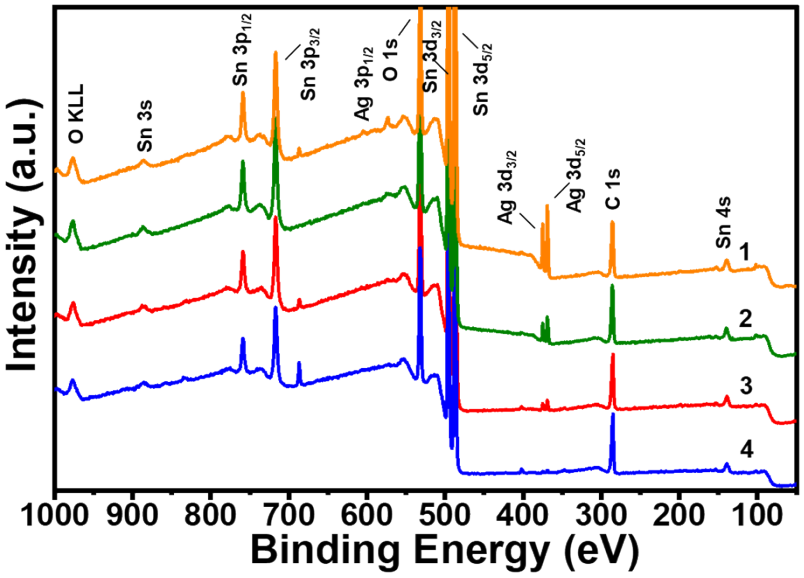

Fig. S4 XPS spectra of different Sn/Ag-y electrodes. The lines of 1, 2, 3, and 4 represent Sn/Ag-10, Sn/Ag-15, Sn/Ag-20 and Sn/Ag-30 electrodes, respectively.

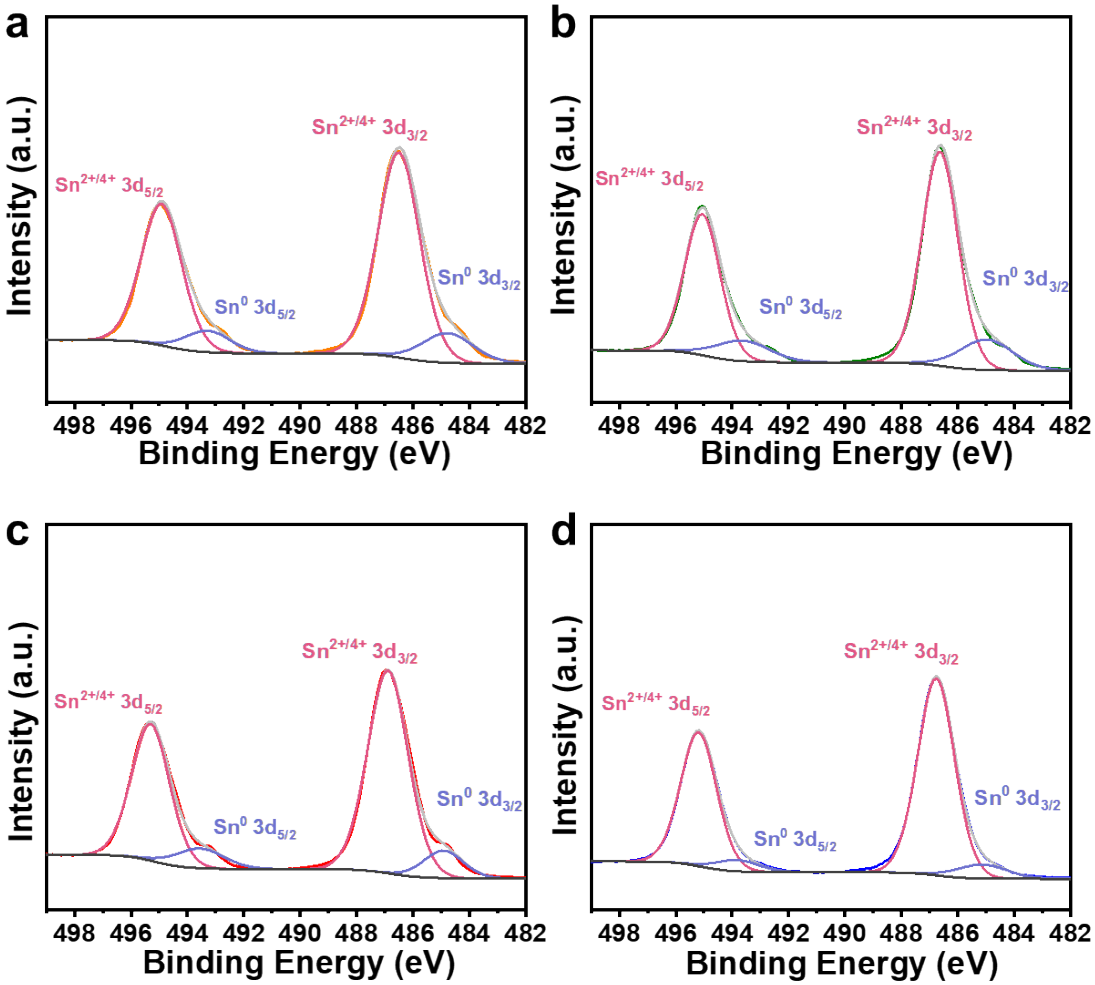

Fig. S5 The high-resolution XPS spectra of Sn 3d: (a) Sn/Ag-10 electrode; (b) Sn/Ag-15 electrode; (c) Sn/Ag-20 electrode; (d) Sn/Ag-30 electrode.

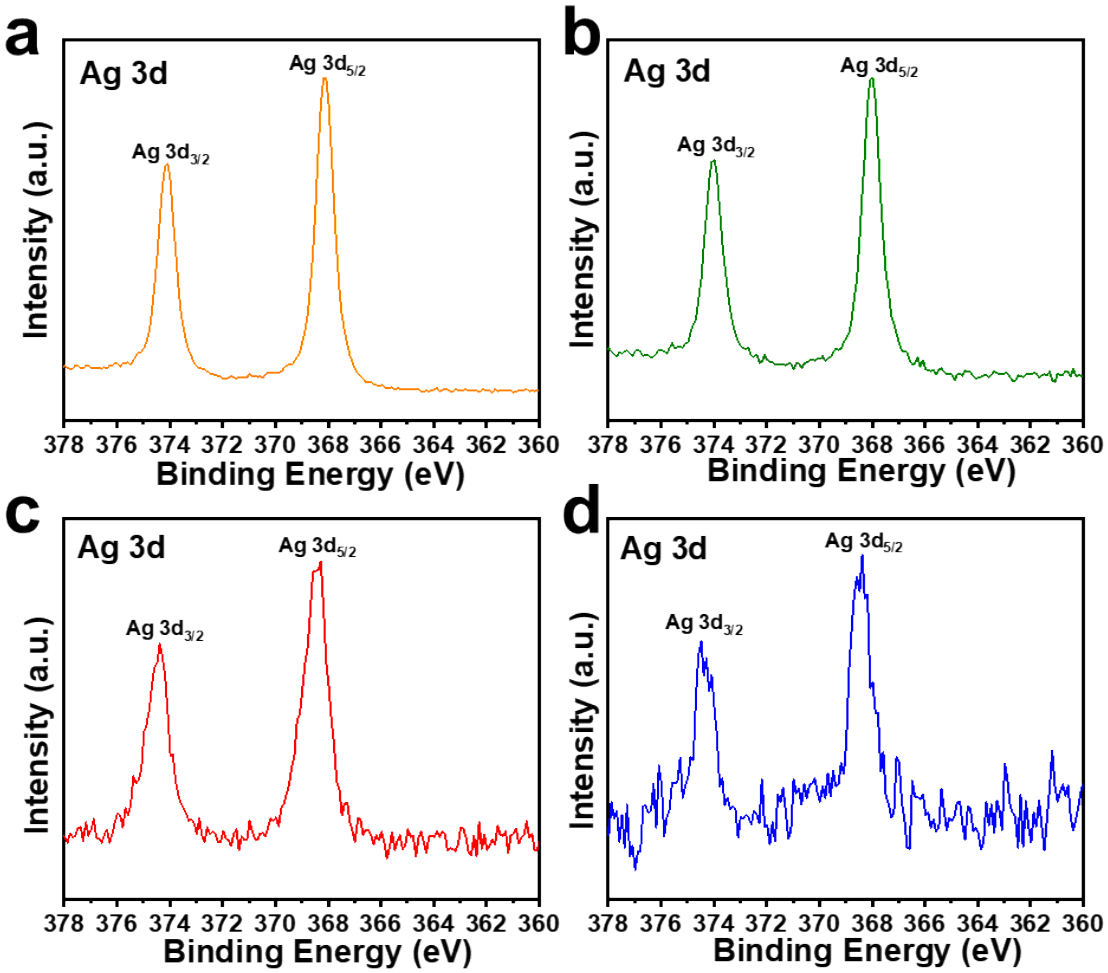

Fig. S6 The high-resolution XPS spectra of Ag 3d: (a) Sn/Ag-10 electrode; (b) Sn/Ag-15 electrode; (c) Sn/Ag-20 electrode; (d) Sn/Ag-30 electrode.

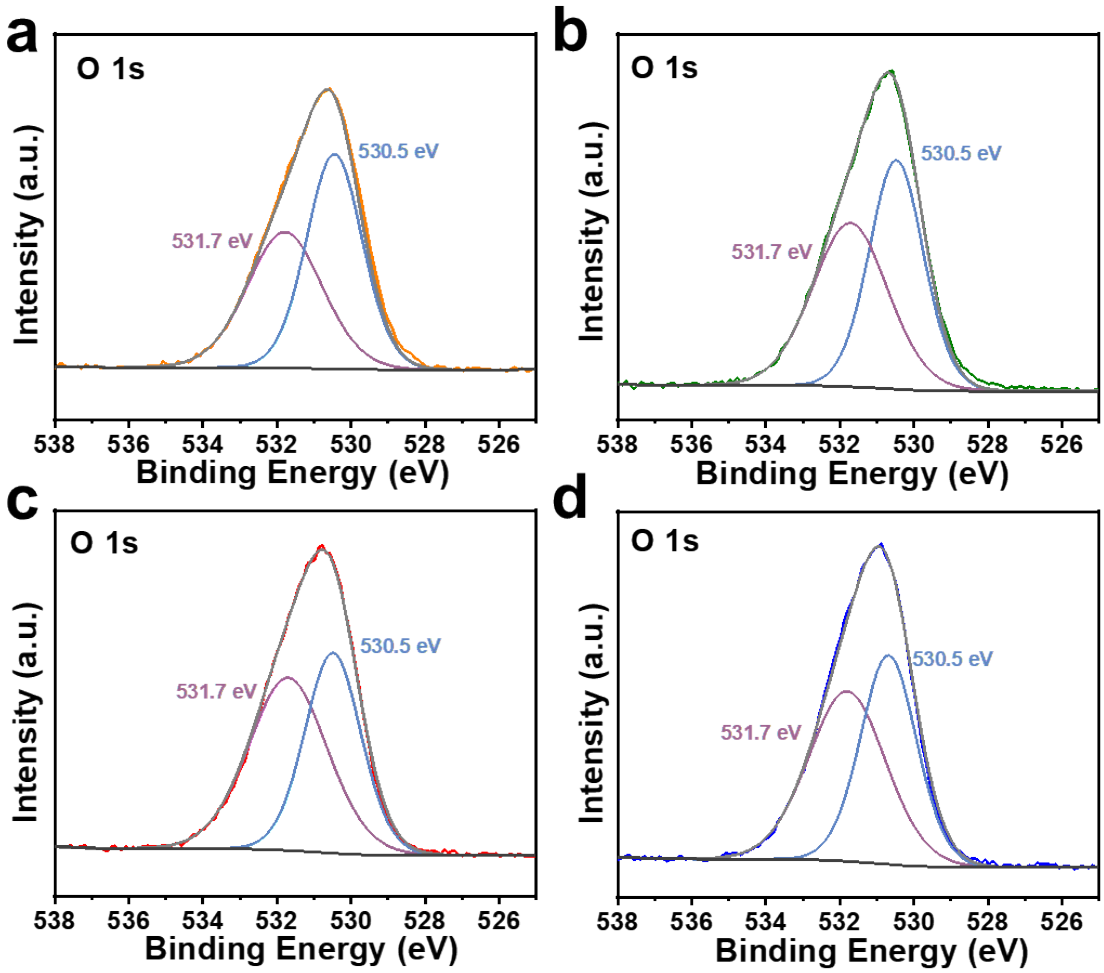

Fig. S7 The high-resolution XPS spectra of O 1s: (a) Sn/Ag-10 electrode; (b) Sn/Ag-15 electrode; (c) Sn/Ag-20 electrode; (d) Sn/Ag-30 electrode.

The high-resolution XPS spectra of O 1s could be fitted into two peaks, signifying two different kinds of oxygen species. The peak with the binding energy at 530.5 eV was attributed to the coordination of oxygen bounded to Sn atoms, and the other peak with the binding energy at 531.7 eV was ascribed to the loss of oxygen[8].

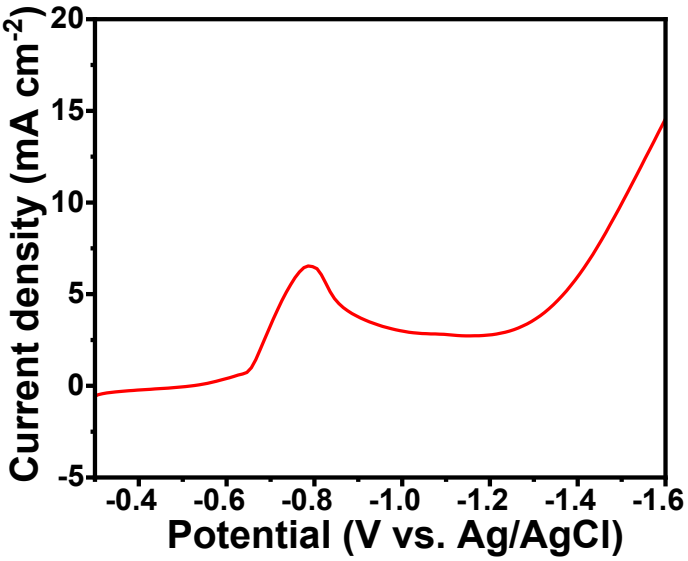

Fig. S8 The LSV trace for the electrodeposition of the Sn/Ag-20 electrode at a scan rate of 20 mV s^{-1}.

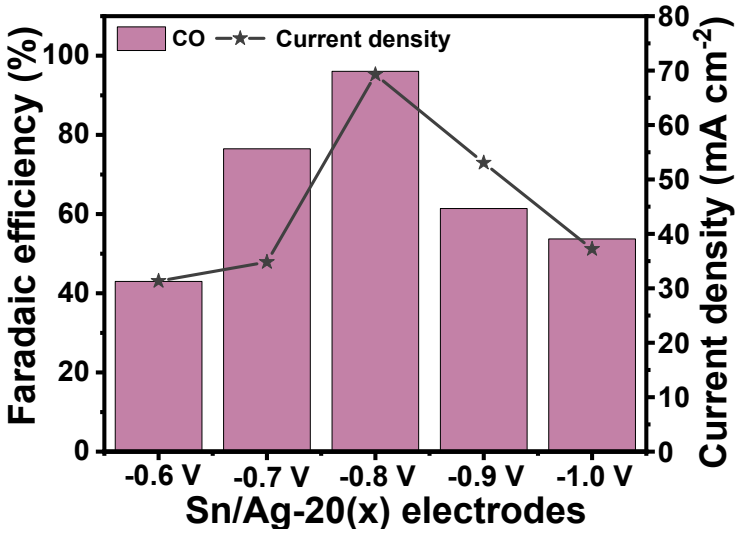

Fig. S9 The current densities of ECR reactions and CO Faradaic efficiencies on different Sn/Ag-20(x) electrodes (x stands for electrodeposition potential). The synthesis method for these Sn/Ag-20(x) electrodes was the same as that of the Sn/Ag-20 electrode, with the exception of a change in the electrodeposition potential.

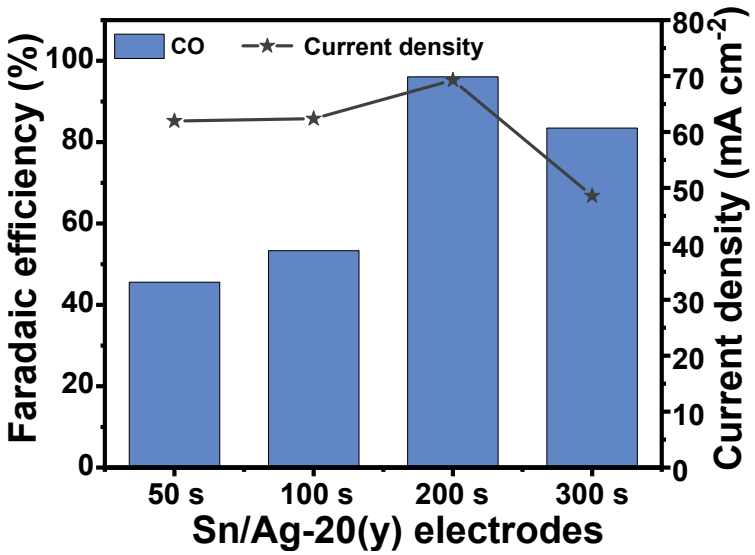

Fig. S10 The current densities of ECR reactions and CO Faradaic efficiencies on various Sn/Ag-20(y) electrodes (y stands for electrodeposition time). The synthesis method for these Sn/Ag-20(y) electrodes was the same as that of the Sn/Ag-20 electrode, with the exception of a change in the electrodeposition time.

The LSV curve in the electrolyte for the electrodeposition is shown in Fig. S8. The reduction peak observed at approximately −0.8 V vs Ag/AgCl was attributed to the reduction of Sn^{2+}. In this study, a series of applied potentials close to −0.8 V vs Ag/AgCl were chosen for the synthesis of various Sn/Ag-20(x) electrodes (x stands for electrodeposition potential). These electrodes were then utilized for the ECR reaction in [Bmim]PF_6 (30 wt.%)/H_2O (5 wt.%)/MeCN electrolytes at −2.3 V vs Ag/Ag^+, and the results are presented in Figure S9. It is evident that the Sn/Ag-20(−0.8 V) electrode obtained at −0.8 V vs Ag/AgCl (*i.e.*, the Sn/Ag-20 electrode) demonstrated the best ECR performance. Additionally, the electrodes prepared with different electrodeposition times at −0.8 V vs Ag/AgCl were also investigated. The obtained Sn/Ag-20(y) (y stands for electrodeposition time) electrodes were subsequently used for the ECR reaction under the same condition. As illustrated in Figure S10, the Sn/Ag-20(200 s) electrode synthesized with a 200 s electrodeposition (*i.e.*, the Sn/Ag-20 electrode) exhibited the highest current density of ECR and the maximum CO Faradaic efficiency.

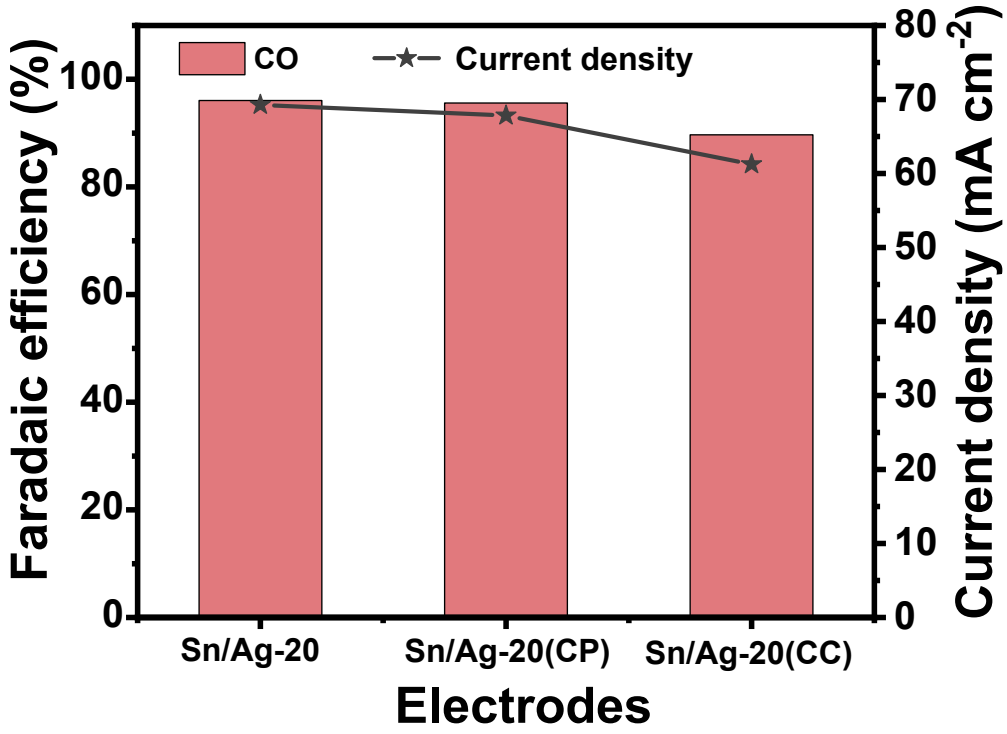

Fig. S11 The current densities of ECR reactions and CO Faradaic efficiencies on Sn/Ag-20(CP) and Sn/Ag-20(CC) electrodes. The synthesis methods for Sn/Ag-20(CP) and Sn/Ag-20(CC) electrodes were the same as that of the Sn/Ag-20 electrode, except for the substitution of the counter electrode with carbon paper (CP) and carbon cloth (CC) during the electrodeposition process.

We also utilized CP and CC as counter electrodes to prepare Sn/Ag-20(CP) and Sn/Ag-20(CC) electrodes, which were then employed as cathodes for ECR reactions. As shown in Figure S11, the current densities of ECR and CO Faradaic efficiencies were similar to that on the Sn/Ag-20 electrode.

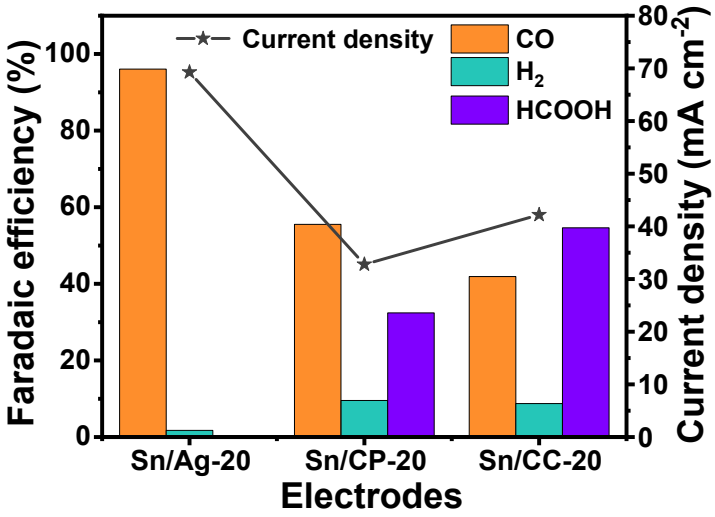

Fig. S12 The current densities of ECR reactions and Faradaic efficiencies of different productions on Sn/Ag-20, Sn/CP-20, and Sn/CC-20 electrodes at −2.3 V vs. Ag/Ag^+. The synthesis methods for Sn/CP-20 and Sn/CC-20 electrodes were the same as that of the Sn/Ag-20 electrode, except for the substitution of the cathode with CP and CC during the electrodeposition process.

The Sn-20 films were also electrodeposited onto bare CP and CC substrates, which were designated as Sn/CP-20 and Sn/CC-20 electrodes, respectively. The Sn/CP-20 and Sn/CC-20 electrodes were then utilized as cathodes for ECR reactions in [Bmim]PF_6 (30 wt.%)/H_2O (5 wt.%)/MeCN electrolytes at −2.3 V vs Ag/Ag^+. As can be observed from Fig. S12, the ECR activities of Sn/CP-20 and Sn/CC-20 electrodes were lower than that of the Sn/Ag-20 electrode, indicating that the Ag substrate is beneficial for promoting the ECR activity.

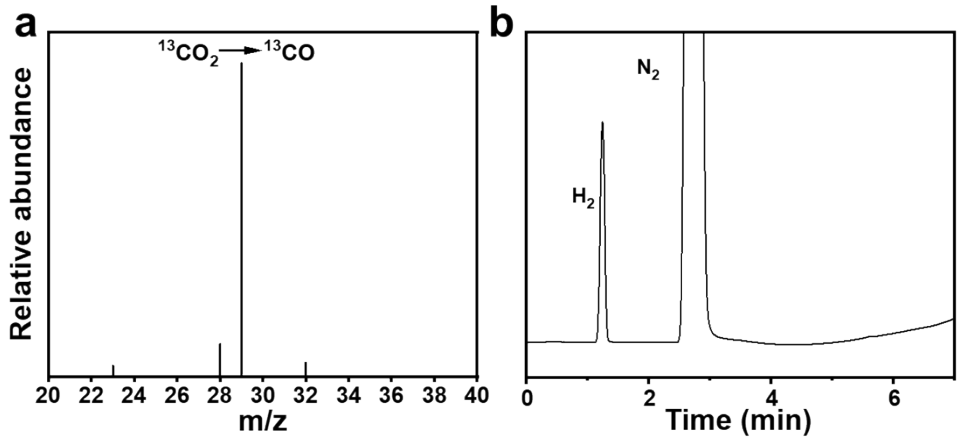

Fig. S13 (a) The mass spectrometry of the isotope labelling experiment for the ECR reaction under $^{13}CO_2$ atmosphere; (b) GC diagram of the reaction gas obtained in a N_2 atmosphere.

To confirm CO source, we utilized isotope-labelled $^{13}CO_2$ (99 at% ^{13}C) and N_2 to replace CO_2 for ECR reactions on the Sn/Ag-20 electrode at −2.3 V vs Ag/Ag^+. After electrolysis experiments, the ^{13}CO was detected using a mass spectrometer in the reaction gas obtained under the $^{13}CO_2$ atmosphere (Fig. S13a), while CO was not observed in the GC chromatogram in the sample obtained under the N_2 atmosphere (Fig. S13b), indicating that the CO was indeed produced from the ECR reaction.

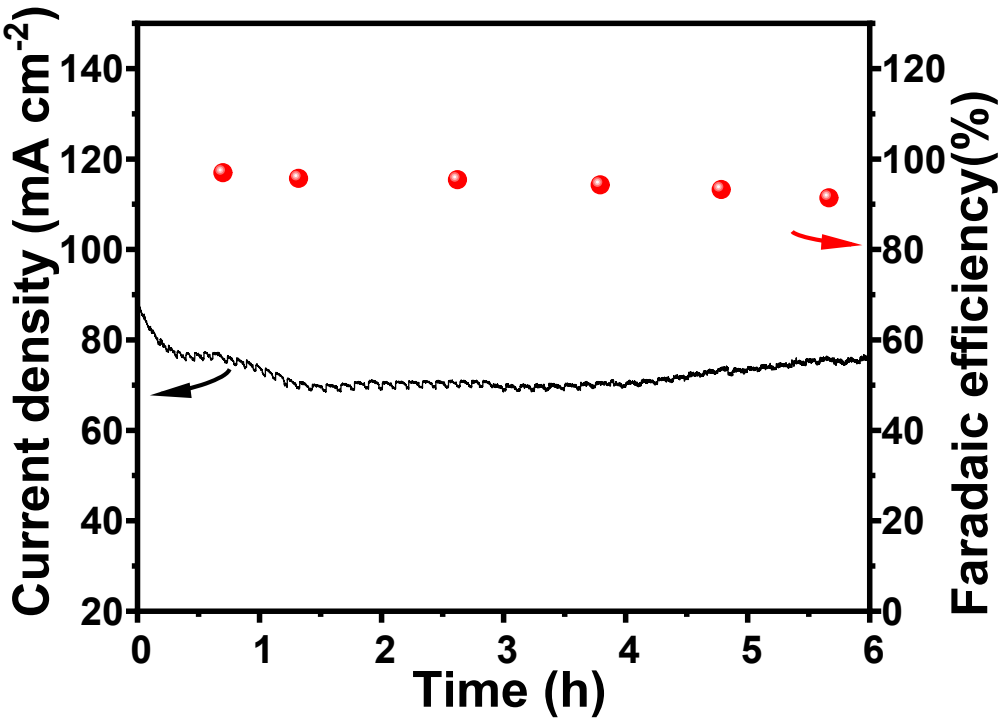

Fig. S14 The i-t curves of the Sn/Ag-20 electrode at -2.3 V versus Ag/Ag^{+}.

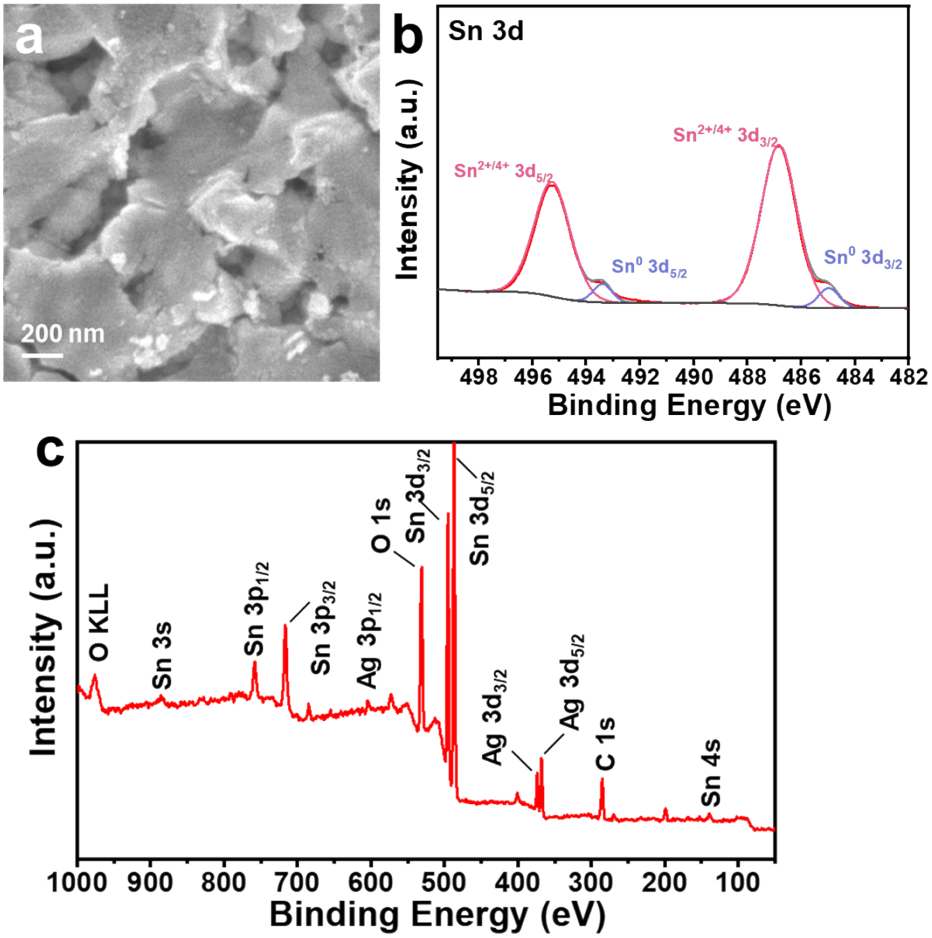

Fig. S15 The characterization of the Sn/Ag-20 electrode after electrolysis: (a) SEM image; (b) The high-resolution Sn 3d XPS spectrum; (c) XPS spectrum.

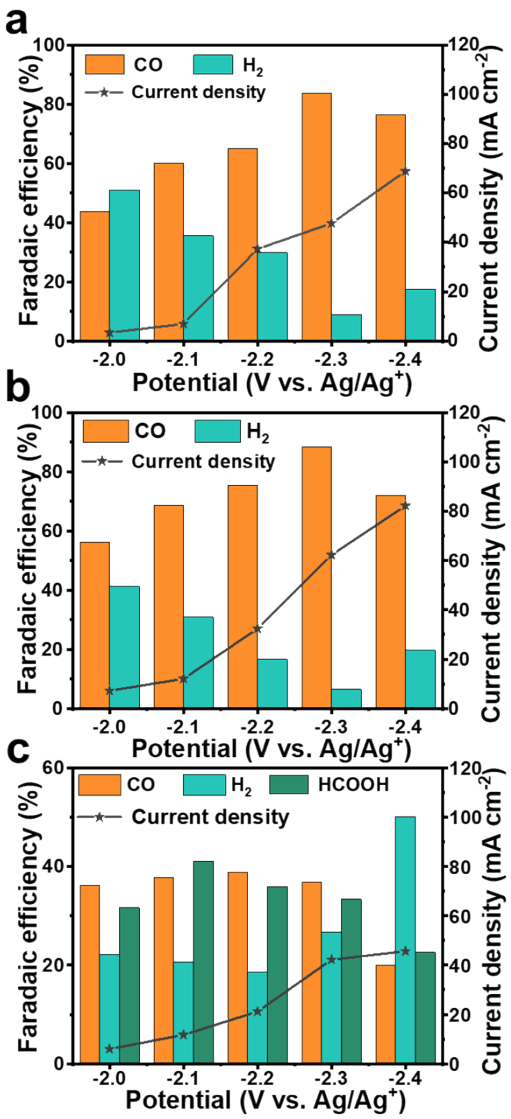

Fig. S16 The current densities of ECR reactions and Faradaic efficiencies of various products on different electrodes: (a) Sn/Ag-10; (b) Sn/Ag-15; (c) Sn/Ag-30.

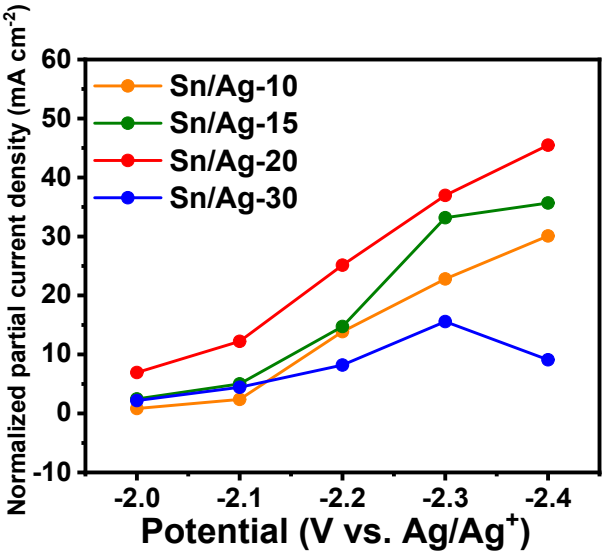

Fig. S17 The normalized CO partial current densities by the corresponding ECSAs over different Sn/Ag-y electrodes at different applied potentials.

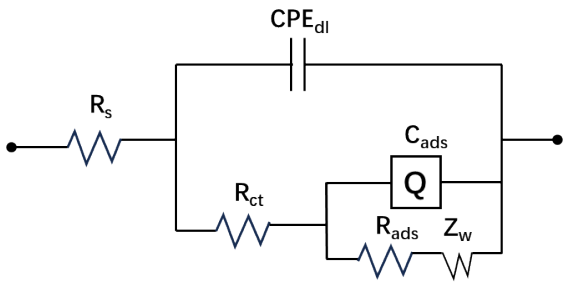

Fig. S18 Randles' equivalent circuit for simulating the experimental impedance data of different Sn/Ag-y electrodes. In the Randles' equivalent circuit, R_s is solution resistance, R_{ct} stands for charge transfer resistance, R_{ads} represents surface adsorption resistance, CPE_{dl} is double layer capacitance, C_{ads} stands for surface adsorption capacitance and Z_w represents Warburg-type impedance.

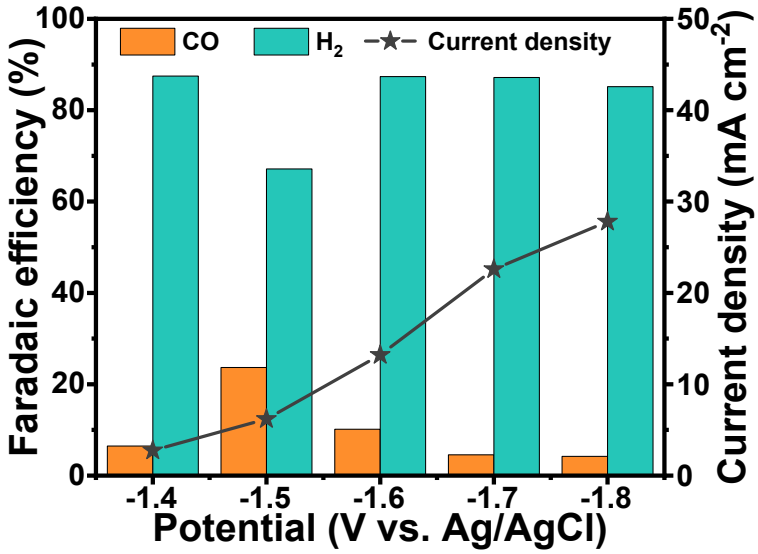

Fig. S19 The current densities of ECR reactions and Faradaic efficiencies of different products on the Sn/Ag-20 electrode in 0.5 M of $KHCO_3$ aqueous solution.

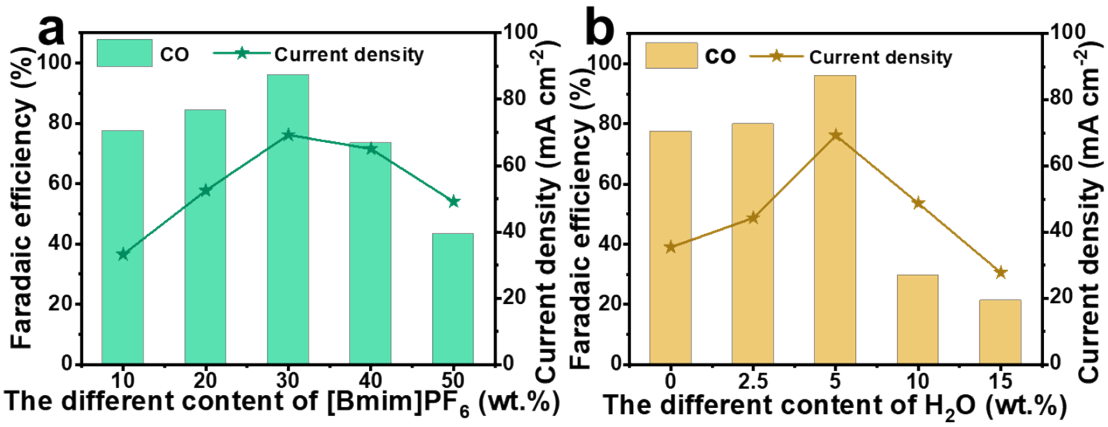

Fig. S20 The current densities of ECR reactions and Faradaic efficiencies of different products on the Sn/Ag-20 electrode in different [Bmim]PF_6/H_2O/MeCN electrolytes: (a) different weight percentage of [Bmim]PF_6 and 5 wt.% of H_2O; (d) different weight percentage of H_2O and 30 wt.% of [Bmim]PF_6.

Table S1. The loading amounts and average thicknesses of Sn-y films on Ag foil surfaces.

Electrode	Loading amount[a] ($mg\ cm^{-2}$)	Average thickness[b] (μm)
Sn/Ag-10	0.1	~8
Sn/Ag-15	0.3	~15
Sn/Ag-20	0.5	~18
Sn/Ag-30	0.6	~23

[a] The loading amount of the Sn-y film on the Ag foil surface was determined as the average of the mass difference of the Ag foil before and after electrodeposition of 10 samples; [b] The average thickness of the Sn-y film on the Ag foil surface was obtained from the cross-sectional SEM image of different electrodes.

Table S2 The atomic ratio of $Sn^{2+/4+}/Sn^0$ and the content of Sn element in different Sn/Ag-y electrodes detected by XPS results.

Electrode	The atomic ratio of $Sn^{2+/4+}/Sn^0$	Sn content (at.%)
Sn/Ag-10	8.7	23.9
Sn/Ag-15	10.0	33.3
Sn/Ag-20	14.7	35.9
Sn/Ag-30	21.3	38.6
Sn/Ag-20 after 6 h electrolysis	13.2	37.9

Table S3 EIS characterization of Sn/Ag-y electrodes. Values of the main parameters of Randles' equivalent circuit elements obtained by fitting the Nyquist plots at open circuit potentials.

Electrode	R_s (Ω)	R_{ct} (Ω)
Sn/Ag-10	4.3	5.9
Sn/Ag-15	4.0	2.8
Sn/Ag-20	3.7	1.6
Sn/Ag-30	5.0	12.8

The electrochemical impedance spectroscopy (EIS) was also carried out in [Bmim]PF_6 (30 wt.%)/H_2O (5 wt.%)/MeCN electrolytes at open circuit potentials (Fig. 3b). The corresponding equivalent circuit and simulated results are provided in Fig. S19 and Table S3. The results indicated that the influence of the $SnCl_2$ concentration in the electrolyte during the electrodeposition process on the R_s value of different Sn/Ag-y electrodes was not considerable. However, the $SnCl_2$ concentration in the electrolyte during the electrodeposition process could change the R_{ct} values of Sn/Ag-y electrodes.

Table S4 The CO Faradaic efficiency and current density of Sn-based nanomaterials for ECR towards CO in the literature.

Electrode	Electrolyte	Potential (V)[a]	Current density (mA cm^{-2})	CO Faradaic efficiency (%)	Ref.
Ag/SnO_2	0.1 M $KHCO_3$	-0.9 V vs. RHE	5.3	99.2	[9]
Ag/Sn	100 mM $[TBA]PF_6$[b] and 100 mM [DBU-H]PF_6[c]	-1.85 V vs. Ag/AgCl	2.6	99	[10]
Ag_{96}/Sn_4	0.1 M $KHCO_3$	-1.2 V vs. RHE	45	100	[11]
SnO/C	0.5 M $KHCO_3$	-0.65 V vs. RHE	8	30	[12]
Cu-SnO	0.1 M $KHCO_3$	-1.1 V vs. RHE	11.5	85	[13]
SnO_x-AgO_x	0.1 M $KHCO_3$	-0.8 V vs. RHE	8	50	[14]
C-Cu/SnO_2-0.8	0.5 M $KHCO_3$	-0.6 V vs. RHE	4.6	93	[15]
Sn_3O_4	0.5 M $KHCO_3$	-0.6 V vs. RHE	16.6	40	[16]
Sn/SnO_x	0.5 M $NaHCO_3$	-0.7 V vs. RHE	3	55	[17]
polycrystalline Sn	0.1 M $KHCO_3$	-0.72 V vs. RHE	0.2	18	[18]
C-SnO_2	0.1 M $KHCO_3$	-0.8 V vs. RHE	2	36	[8]
CuSn NPs/C-A	0.1 M $KHCO_3$	-0.7 V vs. RHE	3	70	[19]
$Sn_{0.3}Ti_{0.7}O_2$	0.5 M $KHCO_3$	-0.6 V vs. RHE	10	94.5	[20]
NP SnO_2	0.1 M $KHCO_3$	-0.89 V vs. RHE	3	40	[21]
Sn/Cu	0.1 M $KHCO_3$	-1.2 V vs. RHE	100	80	[22]
$Cu_{97}Sn_3$	0.5 M $KHCO_3$	-0.7 V vs. RHE	30	98	[23]
Sn/Ag-20	$[Bmim]PF_6$ (30 wt.%)/H_2O (5 wt.%)/MeCN	-2.3 V vs. Ag/Ag^+	69.3	96.0	This work

[a] RHE stands for reversible hydrogen electrode; [b] $[TBA]PF_6$ stands for tetrabutylammonium hexafluorophosphate; [c] [DBU-H]PF_6 stands for 1,8-diazabicyclo[5.4.0]undec-7-ene hexafluorophosphate

Reference

1 B. Ren, G. Wen, R. Gao, D. Luo, Z. Zhang, W. Qiu, Q. Ma, X. Wang, Y. Cui, L. Ricardez–Sandoval, A. Yu and Z. Chen, *Nat. Commun.*, 2022, **13**, 2486.

2 P. Pinthong, S. Phupaichitkun, S. Watmanee, R. Nganglumpoon, D. N. Tungasmita, S. Tungasmita, Y. Boonyongmaneerat, N. Promphet, N. Rodthongkum and J. Panpranot, *Nanomaterials*, 2022, **12**, 3389.

3 S. Gao, Y. Lin, X. Jiao, Y. Sun, Q. Luo, W. Zhang, D. Li, J. Yang and Y. Xie, *Nature*, 2016, **529**, 68-71.

4 G. Wen, D. U. Lee, B. Ren, F. M. Hassan, G. Jiang, Z. P. Cano, J. Gostick, E. Croiset, Z. Bai, L. Yang and Z. Chen, *Adv. Energy Mater.*, 2018, **8**, 1802427.

5 W. Guo, X. Tan, J. Bi, L. Xu, D. Yang, C. Chen, Q. Zhu, J. Ma, A. Tayal, J. Ma, Y. Huang, X. Sun, S. Liu and B. Han, *J. Am. Chem. Soc.*, 2021, **143**, 6877-6885.

6 C. D. Gu, Y. J. Mai, J. P. Zhou, Y. H. You and J. P. Tu, *J. Power Sources*, 2012, **214**, 200-207.

7 W. Luc, C. Collins, S. Wang, H. Xin, K. He, Y. Kang and F. Jiao, *J. Am. Chem. Soc.*, 2017, **139**, 1885-1893.

8 H. Ge, Z. Gu, P. Han, H. Shen, A. M. Al-Enizi, L. Zhang and G. Zheng, *J. Colloid Interface Sci.*, 2018, **531**, 564-569.

9 M. Li, Y. Hu, D. Wang and D. Geng, *Chemistry - An Asian Journal*, 2021, **16**, 2694-2701.

10 T. Kunene, A. Atifi and J. Rosenthal, *ACS Appl. Energy Mater.*, 2021, **4**, 13605-13616.

11 C. Cai, B. Liu, K. Liu, P. Li, J. Fu, Y. Wang, W. Li, C. Tian, Y. Kang, A. Stefancu, H. Li, C. W. Kao, T. S. Chan, Z. Lin, L. Chai, E. Cortés and M. Liu, *Angew. Chem. Int. Ed.*, 2022, **61**, e202212640.

12 J. Gu, F. Heroguel, J. Luterbacher and X. Hu, *Angew. Chem. Int. Ed.*, 2018, **57**, 2943-2947.

13 W. Ju, J. Zeng, K. Bejtka, H. Ma, D. Rentsch, M. Castellino, A. Sacco, C. F. Pirri and C. Battaglia, *ACS Appl. Energy Mater.*, 2018, **2**, 867-872.

14 Y. W. Choi, F. Scholten, I. Sinev and B. Roldan Cuenya, *J. Am. Chem. Soc.*, 2019, **141**, 5261-5266.

15 Q. Li, J. Fu, W. Zhu, Z. Chen, B. Shen, L. Wu, Z. Xi, T. Wang, G. Lu, J. J. Zhu and S. Sun, *J. Am. Chem. Soc.*, 2017, **139**, 4290-4293.

16 Z. Chen, M. R. Gao, N. Duan, J. Zhang, Y.-Q. Zhang, T. Fan, J. Zhang, Y. Dong, J. Li, Q. Liu, X. Yi and J. L. Luo, *Appl. Catal. B Environ.*, 2020, **277**, 119252.

17 Y. Chen and M. W. Kanan, *J. Am. Chem. Soc.*, 2012, **134**, 1986-1989.

18 J. T. Feaster, C. Shi, E. R. Cave, T. Hatsukade, D. N. Abram, K. P. Kuhl, C. Hahn, J. K. Nørskov and T. F. Jaramillo, *ACS Catal.*, 2017, **7**, 4822-4827.

19 P. Wang, M. Qiao, Q. Shao, Y. Pi, X. Zhu, Y. Li and X. Huang, *Nat. Commun.*, 2018, **9**, 4933.

20 G. Wen, B. Ren, M. G. Park, J. Yang, H. Dou, Z. Zhang, Y.-P. Deng, Z. Bai, L. Yang, J. Gostick, G. A. Botton, Y. Hu and Z. Chen, *Angew. Chem. Int. Ed.*, 2020, **59**, 12860-12867.

21 L. Fan, Z. Xia, M. Xu, Y. Lu and Z. Li, *Adv. Funct. Mater.*, 2018, **28**, 1706289.

22 W. Ju, F. Jiang, H. Ma, Z. Pan, Y.-B. Zhao, F. Pagani, D. Rentsch, J. Wang and C. Battaglia, *Adv. Energy Mater.*, 2019, **9**, 1901514.
23 W. Ren, X. Tan, J. Qu, S. Li, J. Li, X. Liu, S. P. Ringer, J. M. Cairney, K. Wang, S. C. Smith and C. Zhao, *Nat. Commun.*, 2021, **12**, 1449.